PROCEEDINGS OF SPIE

SPIEDigitalLibrary.org/conference-proceedings-of-spie

Exoplanet detection with photonic lanterns for focal-plane wavefront sensing and control

Jonathan Lin, Yinzi Xin, Barnaby Norris, Yoo Jung Kim, Steph Sallum, et al.

Jonathan Lin, Yinzi Xin, Barnaby Norris, Yoo Jung Kim, Steph Sallum, Christopher Betters, Sergio Leon-Saval, Julien Lozi, Sebastian Vievard, Oliver Guyon, Pradip Gatkine, Nemanja Jovanovic, Dimitri Mawet, Michael P. Fitzgerald, "Exoplanet detection with photonic lanterns for focal-plane wavefront sensing and control," Proc. SPIE 12185, Adaptive Optics Systems VIII, 121852G (29 August 2022); doi: 10.1117/12.2630692



Event: SPIE Astronomical Telescopes + Instrumentation, 2022, Montréal, Québec, Canada

Exoplanet Detection with Photonic Lanterns for Focal-Plane Wavefront Sensing and Control

Jonathan Lin^a, Yinzi Xin^b, Barnaby Norris^c, Yoo Jung Kim^a, Steph Sallum^d, Christopher Betters^e, Sergio Leon-Saval^e, Julien Lozi^f, Sebastien Vievard^f, Oliver Guyon^{f,g}, Pradip Gatkine^b, Nemanja Jovanovic^b, Dimitri Mawet^b, and Michael P. Fitzgerald^a

^aPhysics & Astronomy Department, University of California, Los Angeles (UCLA), 475 Portola Plaza, Los Angeles, USA

^bDepartment of Astronomy, California Institute of Technology, 1200 E. California Blvd, Pasadena, USA

^cSydney Institute for Astronomy, School of Physics, Physics Road, The University of Sydney, NSW 2006, Australia

^dDepartment of Physics & Astronomy, University of California, Irvine, 4129 Frederick Reines Hall, Irvine, CA 92697 USA

^eSydney Astrophotonic Instrumentation Laboratory, School of Physics, The University of Sydney, Sydney, NSW 2006, Australia

^fSubaru Telescope, 650 N. A'ohoku Place, Hilo, HI 96720 USA ^gUniversity of Arizona Steward Observatory, Tucson, AZ 85721, USA

ABSTRACT

Inner working angle is a key parameter for enabling scientific discovery in direct exoplanet imaging and characterization. Approaches to improving the inner working angle to reach the diffraction limit center on the sensing and control of wavefront errors, starlight suppression via coronagraphy, and differential techniques applied in post-processing. These approaches are ultimately limited by the shot noise of the residual starlight, placing a premium on the ability of the adaptive optics system to sense and control wavefront errors so that the coronagraph can effectively suppress starlight reaching the science focal plane. Photonic lanterns are attractive for use in the science focal plane because of their ability to spatially filter light using a finite basis of accepted modes and effectively couple the results to diffraction-limited spectrometers, providing a compact and cost-effective means to implement post-processing based on spectral diversity. We aim to characterize the ability of photonic lanterns to serve as focal-plane wavefront sensors, allowing the adaptive optics system to control aberrations affecting the science focal plane and reject additional stellar photon noise. By serving as focal-plane wavefront sensors, photonic lanterns can improve sensitivity to exoplanets through both direct and coronagraphic observations. We have studied the sensing capabilities of photonic lanterns in the linear and quadratic regimes with analytical and numerical treatments for different lantern geometries (including non-mode-selective, mode-selective, and hybrid geometries) as a function of port number. In this presentation we report on the sensitivity of such lanterns and comment on the relative suitability and sensitivity impacts of different lantern geometries for focal-plane wavefront sensing.

Keywords: photonic lanterns, wavefront sensing

1. INTRODUCTION

High-contrast imaging is becoming one of the primary tools for the direct detection and characterization of exoplanets. This class of techniques combines ground-based extreme adaptive optics (AO), which corrects for wavefront aberrations induced by passage of light through the atmosphere and the instrument, and coronagraphy,

Further author information:

Jonathan Lin: E-mail: jon880@astro.ucla.edu

Adaptive Optics Systems VIII, edited by Laura Schreiber, Dirk Schmidt, Elise Vernet, Proc. of SPIE Vol. 12185, 121852G ⋅ © 2022 SPIE 0277-786X ⋅ doi: 10.1117/12.2630692

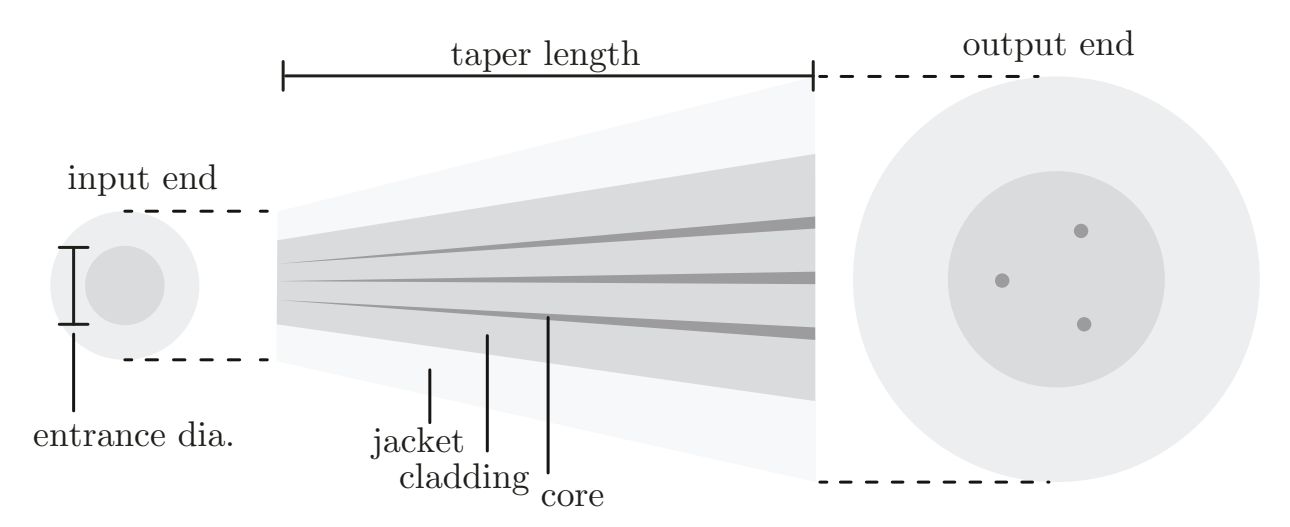


Figure 1. The photonic lantern, a tapered waveguide that can adiabatically transfer light distributed between multiple fiber modes into multiple single-mode cores, or vice-versa. The particular lantern shown above is an idealization of a 3-port lantern, with all jacket, cladding, and core cross-sections assumed to be circular throughout the transition zone. Darker regions indicate higher refractive index. Adapted from.⁷

which suppresses on-axis starlight to reveal the circumstellar environment, as well as contrast-boosting post-processing techniques such as angular differential imaging and spectral differential imaging. Together, these techniques enable contrasts down to $\sim 10^{-6}$ and angular separations down to 200 mas. So far, some 30 exoplanets have been detected through high-contrast imaging techniques; however, almost all are widely separated gas giants with masses several times that of Jupiter. One of the main roadblocks in increasing current sensitivity are non-common-path aberrations (NCPAs): quasi-static aberrations evolving on the timescale of minutes to hours that occur due to instrument instabilities induced by humidity, temperature, and gravity vector changes. Because these aberrations appear downstream from the wavefront sensor, they cannot be removed via typical pupil-plane wavefront control systems. As a result, wavefront control must be improved before instruments can attain the necessary contrasts and angular separations typical for systems similar to the Sun and Earth: $\sim 10^{-10}$ and ~ 100 mas, at a distance of 10 pc, in visible light. One way forward is to sense wavefront aberrations in the focal plane instead of the pupil plane: so-called focal-plane wavefront sensors (FPWFSs) are naturally immune to NCPAs if deployed in or near the science focal plane.

Beyond focal-plane wavefront sensing, a number of new ideas and techniques are being proposed to further advance direct exoplanet characterization. Coherent detection, which exploits the mutual incoherence between planet and star light in order to separate both components. A related technique is nulling interferometry, an alternative to conventional coronagraphy that can achieve smaller inner working angles, and which works by destructively interfering starlight collected from different subapertures or telescopes. In addition to starlight suppression, spectroscopy is required for characterization of exoplanets. The high-resolution spectral analysis of faint objects like exoplanets will require methods for both the efficient coupling of light into the science instrument, and stabilization of that same light, which will vary with time due to passage through the atmosphere and instrument. These two requirements are typically in tension, and thus hard to achieve simultaneously.

The photonic lantern⁸ (PL) provides a platform capable of all of the above (e.g. Lin et al. 2021⁷); other notable applications include OH line suppression through fiber Bragg gratings,^{9,10} and spectroastrometry.¹¹ As seen in Figure 1, the PL is a tapered waveguide that gradually transitions from a multi-mode fiber (MMF) geometry to multiple widely-spaced single-mode cores, similar to a multi-core fiber (MCF), which can then be fanned out to an array of single-mode fibers (SMFs). When the MMF end is placed in the focal plane, the PL can efficiently couple multi-modal telescope light into multiple SMFs. While PLs come in a wide array of port counts and geometries, they can be largely classified into three groups. In what we call the "standard" PL, embedded cores are uniform in structure and refractive index. At the other extreme, "mode-selective" PLs use differing single-mode core radii or index contrasts, so that each fiber mode at the MMF-like lantern entrance

routes to a distinct output port.¹² Lastly, we term lanterns that operate between these two extremes "hybrid lanterns." These lanterns have one core mismatched from the rest, thereby funnelling light from the fundamental fiber mode into a single output port while mixing the remaining light in the rest of the ports.

Critically, in the process of coupling light into an array of SMFs, focal-plane PLs map pupil-plane phase aberrations into intensity variations in a one-to-one manner, at least for small aberrations. This behavior enables the PL to additionally operate as a 100% duty cycle focal-plane WFS.^{13–15} We show an example of this phase-to-intensity mapping in Figure 2, which plots the non-degenerate intensity responses of a 6-port PL in the presence of positive and negative astigmatism. The focus of this work is to assess the performance of the photonic lantern wavefront sensor (PLWFS). PLs are already being considered for use as spectrograph input and coherent detection; in these scenarios, PLs can perform "double duty" by also providing additional focal-plane wavefront sensing. We focus on two contexts the first being fiber-fed, high-resolution spectrometry, mentioned above; and vortex-fiber nulling (VFN), a high contrast imaging technique which exploits symmetries in optical fiber modes to separate star and planet light.¹⁶ In turn, we restrict our analysis to the infrared, since this wavelength regime will be the staging ground for the next push in direct exoplanet spectrometry, with upcoming instruments such as HISPEC and MODHIS.¹⁷

Research in the application of PLs to wavefront sensing is ongoing. For instance, Norris et al. (2020)¹⁴ recently combined a 19-port PL with a neural net to enable non-linear wavefront reconstruction of the first 9 non-piston Zernike modes. In comparison, we take a broader, but less in-depth approach: our goal is to provide a general baseline overview of the capabilities of the PLWFS, as well as the methods through which the sensing properties of these devices might be controlled. We place added emphasis on the linear analysis of the PLWFS, in order to assess the limits of the PLWFS under more standard and simpler linear AO control schemes. In Section §2, we establish the mathematical model that will enable wavefront reconstruction with the PLWFS. First, we expand the PLWFS intensity response to first and second order in phase (§2.1-§2.3). We also consider methods through which these models can be inverted, thereby enabling wavefront sensing. Next, we expand our models to arbitrary modal basis (§2.4): this both increases computational efficiency of the reconstruction models and allows them to be expressed in terms of common phase aberration bases such as the Zernike polynomials. In Section §3, we apply our models to quantify the behavior of the PLWFS. This analysis includes deriving conditions for WFS linearity (§3.1-§3.3), and estimating maximum amount of WFE that can be handles by these sensors (§3.4).

Finally, we combine our models with numerical simulations, to provide a first look at the wavefront-sensing abilities of standard, hybrid, and mode-selective 6-port PLs. Our aim in this work is to develop an initial understanding of the capabilities of the PLWFS, and in doing so we assume "perfect" lanterns and neglect noise sensitivity. We present an overview of our numerical method in §4, and the corresponding results in §5.

2. PROPAGATION ANALYSIS AND PHASE RECONSTRUCTION

2.1 General model

Consider the following general setup for a backend device to an AO-equipped telescope. AO-corrected light passes into an instrument backend, which may contain components such as beam-shaping (PIAA) optics ¹⁸ and additional phase and/or amplitude optics (e.g. vortex fiber nuller mask). After light passes through a number of upstream components, it is focused onto the MMF end of a PL, ultimately propagating into the SMF ports at the PL output. These output ports may also optionally be inteferometrically combined. Because optical propagation is linear in complex electric field, the action of all backend optical components can be lumped into a single complex-valued transfer matrix, which we denote A. This matrix connects the input electric field $E_{\rm in}$ and the output electric field $E_{\rm out}$ of the backend device:

$$E_{\text{out}} = AE_{\text{in}}. (1)$$

In the case of the PLWFS, the transfer matrix A will contain a projection component, since an N-port lantern will (generally speaking) support only N complex-valued electric field modes, meaning that the vector \mathbf{E}_{out} is N-dimensional. Note that, unlike the modes of a standard optical fiber, the modes of a PL correspond to three-dimensional light distribution functions, encompassing the full propagation of light from the MMF-like

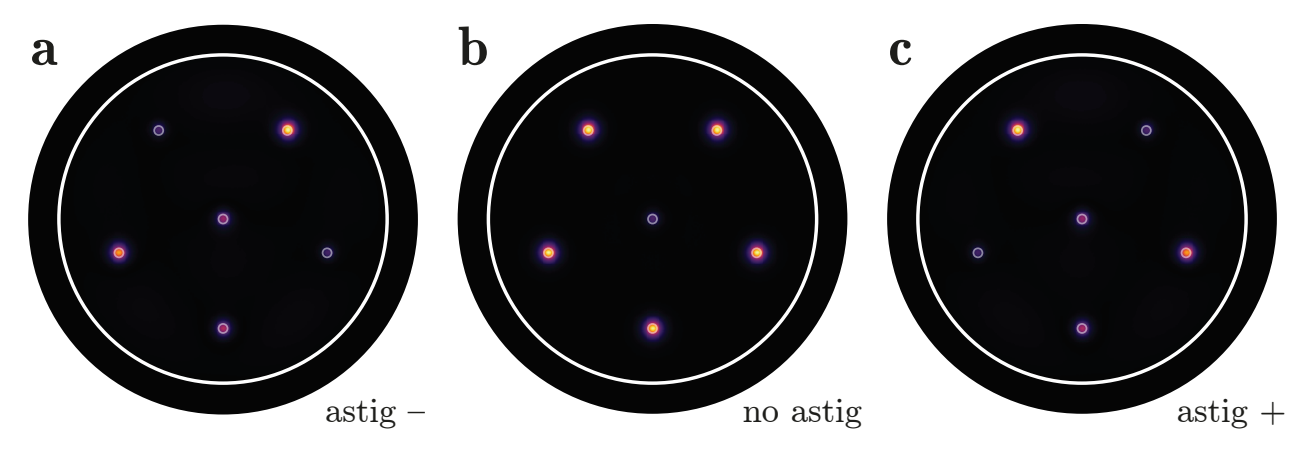


Figure 2. Simulated response of a 6 port lantern in the presence a: -1 rad rms astigmatism; b: 0 rad rms astigmatism; and c: +1 rad rms astigmatism. The photonic lantern converts phase variations into unique intensity variations among the output cores. Circles show the jacket-cladding interface and the cladding-core interfaces. Optical propagation is simulated using the Python packages HCIPy and Lightbeam.

input to the MCF-like output of the lantern. Here, we have a choice of mode basis. The modes we use in this work, which we term "lantern modes," look like individual SMF modes at the lantern exit, and complex linear combinations of linearly polarized (LP^{19}) fiber modes at the lantern entrance. These modes can be computed by illuminating a single output core at the lantern exit and numerically back-propagating light to the lantern entrance. Simulated cross-sections of lantern modes at the PL entrance, computed in this manner, are shown in Figure 3 for a standard 6-port lantern. The action of the A matrix is to simulate optical propagation through the telescope and any subsequent beam-shaping to the PL entrance, and then project the focal plane electric field onto these lantern modes. Accordingly, A has dimensions $N \times M$, for an N-port lantern and M pupil samples.

Since we ultimately measure intensity, not complex amplitude, we recast equation 1 in terms of the intensity response I_{out} :

$$I_{\text{out}} = |AE_{\text{in}}|^2. \tag{2}$$

The general goal of wavefront sensing is to invert equation 2. We go over methods to do so in the following subsections.

2.2 Linearizing the intensity response

In this subsection, we provide a review of wavefront sensing in the linear regime. While optical propagation is linear in complex amplitude, it is non-linear in intensity. However, in the presence of small aberrations, the intensity response will vary in a near-linear manner. Consider a phase-only aberration ϕ in an electric field with assumed uniform intensity $I_{\rm in}=1$. For small aberrations, we can make the approximation

$$E_{\rm in} = \exp(i\phi) \approx 1 + i\phi \tag{3}$$

where the vector $\mathbf{1}$ represents the electric field of a flat wavefront. The intensity resulting from the phase aberration $\boldsymbol{\phi}$ is

$$I_{\text{out}} = |AE_{\text{in}}|^2,$$

$$\approx |A(\mathbf{1} + i\phi)|^2$$

$$I_{\text{out}} \approx |A\mathbf{1}|^2 + 2\operatorname{Im}\left[(A\mathbf{1}) \odot (A^*\phi)\right]$$
(4)

where the squaring and (||) operators are element-wise, (\odot) represents element-wise (Hadamard) multiplication, and Im denotes taking the imaginary part. We can define the matrix B, having the same dimensions as A, as

$$B_{ij} \equiv 2 \operatorname{Im} \left[A_{ij}^* \sum_k A_{ik} \right] \tag{5}$$

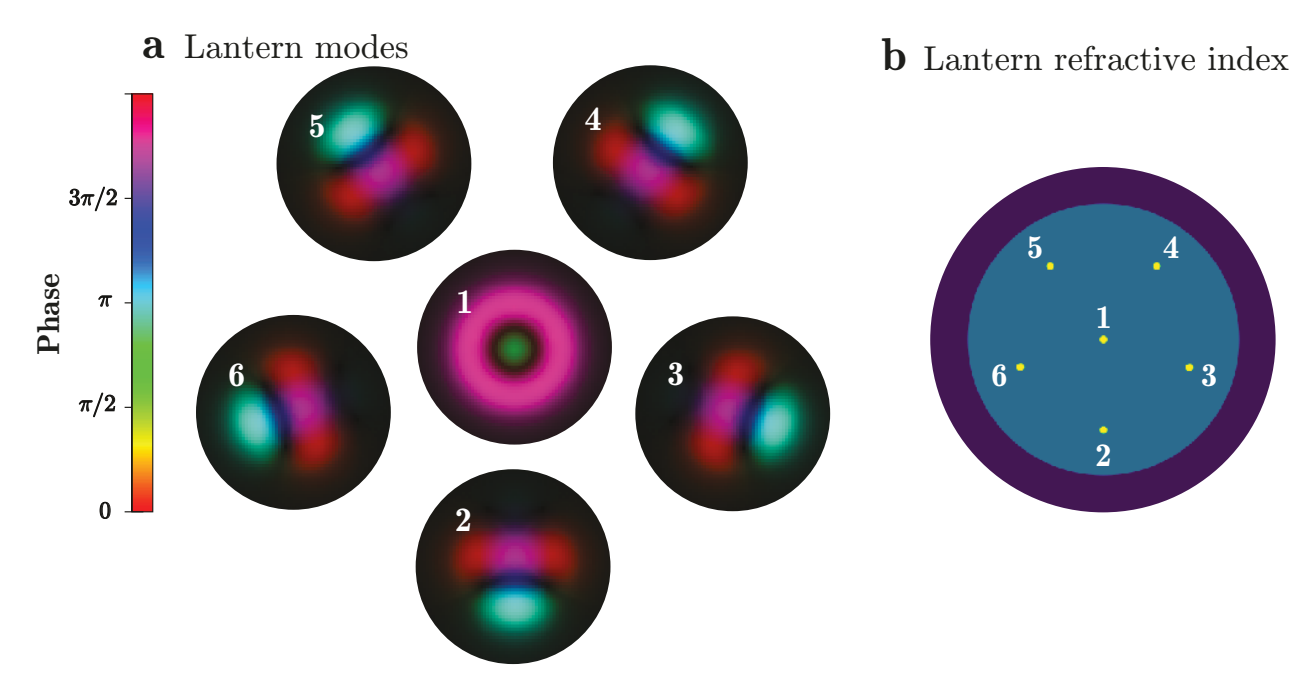


Figure 3. Panel a: Lantern modes for the same 6-port lantern as in Figure 2. Phase is plotted in color, while amplitude is plotted in opacity. The 6 lantern modes are oriented to reflect the location of their corresponding lantern ports, shown on the right. To identify the ports and lantern modes, we index them according to the numerical labels. Panel b: the refractive index profile of the output (MCF-like) end of the PL. Embedded SMF cores are shown in yellow. Numerical labels connect each core to its corresponding lantern mode in panel a.

and recover

$$I_{\text{out}} \approx |A\mathbf{1}|^2 + B\boldsymbol{\phi}.$$
 (6)

We see that the quantity $|A\mathbf{1}|^2$ represents the bias intensity when there is no phase error, while the matrix B (often called the "interaction matrix" in the context of adaptive optics) describes the linear response of the intensities to phase perturbations from the perfect wave. Equation 6 can be inverted (e.g. via Moore-Penrose pseudo-inverse), enabling the reconstruction of phase errors from intensity responses. The phase aberration modes which this backend device can sense in the linear regime will be determined by the B matrix; un-sensed aberration modes will lie in the null space of B.

2.3 Second-order analysis of intensity response

Under perfect knowledge of the system transfer matrix A, we may attain greater accuracy by expanding WFS response to second order. The incident electric field is then approximated as

$$E_{\rm in} \approx 1 + i\phi - \frac{1}{2}\phi^2.$$
 (7)

Repeating the analysis of the previous subsection leads to the following:

$$I_{\text{out}} = |A\mathbf{1}|^2 + 2\text{Im} \left[(A\mathbf{1}) \odot (A^* \phi) \right] - \text{Re} \left[(A\mathbf{1}) \odot (A^* \phi^2) \right] + |A\phi|^2.$$
 (8)

We define the matrix C as

$$C_{ij} \equiv 2\sum_{k} \operatorname{Re}\left[A_{ij}^* A_{ik}\right] \tag{9}$$

where Re denotes taking the real part. This yields the following formula for how phase errors up to second order affect intensity:

$$I_{\text{out}} \approx |A\mathbf{1}|^2 + B\phi - \frac{1}{2}C\phi^2 + |A\phi|^2.$$
 (10)

Inversion of equation 10 can be accomplished using root-finding methods such as Newton-Raphson. Such methods often benefit from knowledge of the Jacobian, which can be derived from equation 10:

$$J_{ij} = \frac{\partial I_{\text{out},i}}{\partial \phi_j} = B_{ij} + (|A_{ij}|^2 - C_{ij})\phi_j + \sum_k A_{ij} A_{ik}^* \phi_k.$$
 (11)

However, it is important to note that inversion of quadratic and higher-order models is more complicated, primarily because such models can admit multiple solutions. This multiplicity may be a real property of the WFS system, or an artifact due to truncation of the power series. We briefly discuss how the issues may be mitigated in §5.3.

2.4 Modal basis

The matrices A, B, and C will each have N by M entries, where N is the number of output ports and M is the number of sample points in the pupil plane. This is computationally inefficient — the number of sample points will almost always greatly exceed the number of lantern ports, making the above matrices unnecessarily large. It is more efficient to represent phase aberrations in terms of some modal basis (e.g. Zernike modes, lantern modes as projected onto pupil phase, or Karhunen-Loève modes derived from second-order phase aberration statistics). To do so, write the phase aberration vector ϕ as

$$\phi = Ra, \tag{12}$$

where a is the real-valued vector of modal coefficients and R is the change-of-basis-matrix, whose columns correspond to the basis vectors. Defining $B' \equiv BR$, the linear model given by equation 6 is easily extended to modal basis as follows:

$$I_{\text{out}} \approx |A\mathbf{1}|^2 + B'\mathbf{a}. \tag{13}$$

Extension of the quadratic model to modal basis is more involved. Inserting equation 12 into equation 10 results in the following:

$$I_{\text{out},i} \approx |A\mathbf{1}|_i^2 + (B'\mathbf{a})_i - \frac{1}{2} \sum_{jk} C'_{ijk} a_j a_k + |A'\mathbf{a}|_i^2$$
 (14)

where the tensor C' is defined as

$$C'_{imn} \equiv 2\sum_{j} \operatorname{Re}\left[A_{ij}^{*} \sum_{k} A_{ik}\right] R_{jm} R_{jn}.$$
(15)

Differentiating equation 14 yields the Jacobian, under the quadratic approximation, in terms of modal basis:

$$J'_{ij} = B'_{ij} + \sum_{k} \left(\text{Re} \left[A'_{ij} A'^*_{ik} \right] - \frac{1}{2} C'_{ijk} \right) a_k + \left[|A'_{ij}|^2 - \frac{1}{2} C'_{ijj} \right] a_j.$$
 (16)

3. PLWFS PROPERTIES

In this section, we provide an initial analysis of the wavefront-sensing properties of the PLWFS. We denote $E_{\rm in}$ and $E_{\rm out}$ as the input electric field (located in the pupil-plane) and output electric field (located at the backend of lantern), respectively, of the overall telescope-PLWFS system. Following the analysis of the previous section, $E_{\rm in}$ and $E_{\rm out}$ are related by the complex-valued transfer matrix A. Additionally, we assume that there is no modal attenuation (flux loss) during propagation through the PL. We expand the A matrix as

$$\boldsymbol{E}_{\text{out}} = UPF\boldsymbol{E}_{\text{in}}.\tag{17}$$

Here, $F \propto -i\mathcal{F}$ is the Fraunhofer propagator, where \mathcal{F} is the Fourier transform; P is the real-valued projection matrix that converts the focal-plane electric field into LP mode amplitudes; and U is the unitary matrix representing propagation through the lantern. In other words, U transforms a focal-plane electric field, expressed in

terms of LP mode amplitudes, into a set of complex-valued SMF amplitudes. Let us further assume phase-only aberrations. Expanding the complex exponential with Euler's identity yields

$$E_{\rm in} = T\cos\phi + iT\sin\phi \tag{18}$$

where T is the real-valued transmission mask of the pupil. Vector-vector multiplication is assumed element-wise. We now derive some results.

3.1 Impact of perfect mode selectivity

In this section, we show that for an even pupil transmission T, a perfect mode-selective lantern (where each fiber mode maps to a distinct output port) maps $\pm \phi$ to the same intensity response. First, note that for perfect mode-selectivity, the lantern propagation matrix U is the identity matrix. Therefore, the complex response of the system for a positive and negative phase aberration is

$$E_{\text{out}}(\pm \phi) = -iP\mathcal{F} \left[\mathbf{T} \cos \phi \pm i \mathbf{T} \sin \phi \right]$$
$$= -iP \left[\mathbf{a} \pm i \mathbf{b} \right]$$
(19)

where we have defined

$$\mathbf{a} \equiv \mathcal{F} \left[\mathbf{T} \cos \phi \right], \mathbf{b} \equiv \mathcal{F} \left[\mathbf{T} \sin \phi \right].$$
(20)

We now make use of the following properties of the Fourier transform:

- 1. The Fourier transform of a real, even function is real and even.
- 2. The Fourier transform of a real, odd function is imaginary and odd.

First, consider ϕ even. In this case, due to the Fourier transform properties, the real-ness of ϕ , and the symmetry properties of composite functions, both a and b are real and even. Therefore, the intensity response is

$$I_{\text{out}}(\pm \phi_{\text{even}}) = |E_{\text{out}}(\pm \phi_{\text{even}})|^2 = (Pa)^2 + (Pb)^2. \tag{21}$$

For even phase aberrations, the intensity response of a mode-selective PLWFS is even. Next, consider odd phase aberrations. Repeating a similar analysis, we now find that while a is still real and even, b is now odd and imaginary. Therefore,

$$I_{\text{out}}(\pm \phi_{\text{odd}}) = |E_{\text{out}}(\pm \phi_{\text{odd}})|^2 = (Pa)^2 + (iPb)^2 \pm 2(Pa) \odot (iPb). \tag{22}$$

While an even phase aberration produces a real and imaginary field component, an odd phase aberration produces two real field components that interfere with each other. Under certain circumstances, this interference can break sign ambiguity. However, for the PLWFS, the vectors \boldsymbol{a} and \boldsymbol{b} are ultimately projected by P onto the LP mode basis: a basis of real-valued, even and odd electric field distributions. As a result, the last term in equation 22 is always 0. This is because \boldsymbol{a} is even, and only has non-zero overlap with even modes, while \boldsymbol{b} is odd, and only has non-zero overlap with odd modes. Finally, since any field can be decomposed into an even and odd component, the intensity response of the mode-selective PLWFS is even for all $\boldsymbol{\phi}$, at least in the vicinity of the origin.

As a corollary, the above implies that mode-selective lanterns have a linear response matrix B=0.

3.2 Non-mode-selectivity can break sign ambiguity

For a non-mode-selective lantern, the matrix U is not the identity matrix; the rows of the matrix UP are the (complex-conjugated) lantern modes. We repeat the analysis from the prior section. The intensity response is

$$I_{\text{out}}(\pm \phi) = |E_{\text{out}}(\pm \phi)|^2 = |UP(a \pm ib)|^2.$$
(23)

From the above, we see sign ambiguity is broken. The matrix U applies a "rotation" to the vector Pa + iPb. While this rotation preserves the overall norm of the vector, it alters the modulus of the individual elements, and hence, the powers in the individual ports of the PLWFS.

In other words, switching the sign of a phase aberration is equivalent to conjugating the complex response of the telescope. If we immediately measure the focal plane electric field in the LP mode basis, this conjugation cannot be detected. However, if we apply a unitary transformation (e.g. a PL) after this conjugation, and then measure, the conjugation can be detected.

3.3 Conditions for linearity

In this section we derive criteria that the PLWFS must meet to maximize linear sensitivity to a given mode. We will restrict ourselves to the second-order expansion of intensity response for the PLWFS, equation 10.

To maximize the linear response of the PLWFS for a particular aberration mode, denoted by unit vector \hat{z}_i , we require that the linear term in equation 10 is maximized and the quadratic terms are minimized. We can encourage this behavior by demanding that the quantity

$$Q \equiv [A\mathbf{1} \odot (A\hat{\mathbf{z}}_i)^*] \tag{24}$$

is purely imaginary. Repeating the same expansion of A from the prior subsections, we equivalently require that

$$Q \equiv [UP\mathcal{F}1 \odot (UP\mathcal{F}\hat{z}_i)^*] \tag{25}$$

is purely imaginary. To connect with the analysis of §2.2, note that $B\hat{z}_i = 2 \text{ Im } Q$. Ultimately, linearity imposes a phase restriction on Q: linear response is maximized when Q is purely imaginary, and minimized when Q is purely real. Note that this maximization specifically affects only linearity about the origin; it is not a maximization of linear range, although it is likely the first step in an analytically-informed optimization of the latter.

Optimization for the above metric can be tricky, but can be simplified in certain cases. In Appendix A, we simplify the above linearity condition for a standard 6-port lantern in the presence of defocus.

3.4 WFS limitations

Even with a perfect non-linear reconstruction model, wavefront sensing breaks down when two distinct phase aberrations can map to the same WFS response. These "degenerate" aberrations are not a concern when the WFS is operating in the linear regime and the mapping of aberrations to sensor intensity responses is one-to-one, but become increasingly problematic as the amplitude of phase aberrations increases. A way to estimate when degenerate aberrations may become problematic is to find where, for some given input wavefront aberration, the corresponding column of the Jacobian becomes zero-valued. This estimation is conservative, as the measurements can still carry information about the input WFE even in the presence of a small amount of degeneracy.

Mathematically, we look for aberrations a_0 for which a column of the Jacobian evaluates to 0:

$$\left. \frac{\partial \mathbf{I}_{\text{out}}}{\partial a_j} \right|_{\mathbf{a}_0} = 0. \tag{26}$$

To motivate this criterion, suppose we find some aberration a_0 where the above criterion is fulfilled. In turn, the WFS response about a_0 , in the a_j direction, may behave quadratically:

$$I_{\text{out}}(a_{0,k} + a_j) = I_{\text{out}}(a_{0,k}) + \frac{I''_{\text{out}}(a_{0,j})}{2} a_j^2 + o\left(a_j^3\right).$$
(27)

Here, $a_{0,j}$ is the j_{th} element of \mathbf{a}_0 . We immediately see that for small a_j , aberrations $a_{0,j} \pm a_j$ map to the same intensity response. More widely separated pairs of degenerate aberrations may also occur around \mathbf{a}_0 , although they most likely will not be positioned symmetrically about $a_{0,j}$. For an alternative perspective, consider the

modal-basis representation of the Jacobian, which has dimensions N rows by M columns for N lantern ports and M aberration modes, with $N \ge M$. The zeroing of a column makes the Jacobian rank-deficient, implying that locally about \mathbf{a}_0 , the mapping of phase aberrations to PL intensity outputs can no longer be injective. In other words, we are guaranteed scenarios where two or more distinct phase aberrations map to the same intensity response.

The norm (or total RMS WFE) of the smallest aberration vector a_0 which satisfies 26 sets the scale in phase aberration space beyond which degeneracy can occur. We term this scale the "degenerate radius." Note that this way of measuring the degenerate radius is conservative, because we do not explicitly check if the quadratic term in the series expansion 27 is non-zero. To actually compute the degenerate radius, we take a numerical approach: feeding a standard root-solving algorithm (e.g. Levenberg-Marquardt) a series of random initial guesses in the vicinity of the origin, repeatedly solving 26, and then taking the solution with the smallest norm from the returned set. In this approach, we require the full form of the Jacobian for the WFS, without any power series approximations. We derive the following form for the Jacobian:

$$\frac{\partial (I_{\text{out},i}/I_{\text{in}})}{\partial a_k} = -2 \operatorname{Im} \left[\sum_j A_{ij} e^{i\phi_j} R_{jk} (1 - a_k) \times \sum_{j'} A_{ij'}^* e^{-i\phi_{j'}} \right]. \tag{28}$$

Here, $\phi \equiv Ra$, as in section §2.4. A rougher but simpler approximation for the degenerate radius can be made by expanding wavefront response only to second-order: essentially, we set equation 16 equal to 0, for fixed aberration index j. This conveniently gives an ordinary matrix-vector equation which can be solved quickly and directly using the Moore-Penrose pseudo-inverse, giving exactly one solution a_0 per aberration. However, this approach can be inaccurate if the WFS response contains little quadratic component.

Lastly, we consider the maximum number of modes that an N-port lantern can sense. In the linear model, it is clear that such a lantern at most can sense N aberration modes. However, this limit holds for non-linear models as well. This is because our optical system, while non-linear in intensity, is linear in complex amplitude. A lantern attempting to sense more aberration modes than it has ports is guaranteed to map two distinct phase aberrations to the same complex-valued lantern response, and in turn, the same real-valued intensity. Topological theorems, such as invariance of domain, lead to the same conclusion. In Lin et al. (in prep),²⁰ we show that this limitation is likely conservative; numerical results imply that N-port PLs can sense at most N-1 modes, without additional optics.

4. SIMULATIONS

In order to provide the initial steps for general characterization of the PLWFS, we simulate these devices using a numerical model in Python. This model has three primary components: a telescope model, which takes in an incident wavefront and returns a focal plane electric field; a PL propagator, which takes both a focal plane electric field and a lantern geometry, and returns the resulting power distribution of the output ports; and wavefront reconstructer, based on the analysis in Section §2. Sections §4.1, §4.2, and §4.3 expand upon these components, respectively. Finally Section §4.4 goes over the specific 6-port PL geometries which we simulate with our numerical model.

4.1 Telescope simulation

Propagation through telescope optics is handled using the HCIPy package. Simulations are monochromatic, at a wavelength of 1.55 μ m. We additionally assume a 10 m circular, unobstructed aperture; the focal ratio of the system is optimized to ultimately maximize coupling of an unaberrated wavefront into the PL. Pupil-to-focal plane propagation is handled via HCIPy's Fraunhofer propagator.

4.2 Lantern propagation

After computing the focal-plane electric field distribution, the most straightforward way to determine the overall intensity response is to numerically propagate the field through the lantern. However, this method computationally inefficient, since it requires a separate beam propagation every time the electric field changes. Instead, we

compute the lantern modes for a given PL design by illuminating each single-mode port at the lantern output with its fundamental mode and using the Lightbeam Python package²² to backpropagate that light to the MMF-like lantern entrance. With the lantern modes in hand, we can determine the amount of power that ultimately ends up in each port by computing overlap integrals between corresponding lantern modes and the focal-plane electric field.

4.3 Wavefront reconstruction

Given some PLWFS intensity response, we may now attempt to reconstruct the original phase aberration. Critically, to simplify our models, we neglect the impact of noise; the treatment of noise, and related analyses of PLWFS sensitivity, are left for future work. In the meantime, our noise-less model will still be useful for an initial characterization of PLWFS capabilities. Our reconstruction model is as follows.

First, we expand phase aberrations in terms of the Zernike basis. To implement linear reconstruction, we compute the matrix B' from equation 13; this is done by numerically measuring the matrix of slopes $\partial I_i/\partial a_j$ about the origin. Here, I_i denotes the intensity of the i_{th} output port and a_j denotes the amplitude of the j_{th} Zernike mode, in radians RMS. We then calculate the Moore-Penrose pseudo-inverse of B', which enables inversion of equation 13. Note that this reconstruction method neglects any sort of flux normalization, which is unnecessary in the context of simulations but may be more desirable in a more practical implementation with real optics.

In contrast, quadratic reconstruction requires knowledge of the A matrix, equation 10, which can then be used to compute the modal-basis matrices A' and B', and the tensor C'. The A matrix is computed by probing the pupil-plane electric field (resolved into a 128 by 128 grid of samples) pixel-by-pixel, and measuring the complex-valued response of the PLWFS. This is straightforward in the case of simulations, since the complex-valued electric field is known. In contrast, experimental measurement of the A matrix will likely require some phase-diversity method. Inversion of the quadratic model, equation 14, is handled using the Levenberg-Marquardt root-finding algorithm, as implemented by the Python package SciPy. We set the starting point of the root-finding routine to the linearly-reconstructed wavefront aberration.

4.4 Simulated lanterns

To demonstrate the validity of our mathematical analysis, we simulate wavefront reconstruction with two types of 6-port PL: standard and hybrid. Both PLs obey the following assumptions. Firstly, we assume that PLs taper uniformly and linearly so that cross sections of the cores and overall cladding of a PL remain perfectly circular throughout the transition zone. While this is an idealization, it remains a useful starting point for a first-order analysis of the PLWFS, especially since it is unclear whether PL imperfections (such the non-circular claddings exhibited by PLs formed via the tapering of SMF bundles) will dampen or promote sensing performance.

Beyond the above idealization, we assume that all PLs taper by a factor of 8 from entrance to exit, with cores spaced in the cladding in such a way that is consistent with the geometries produced when constructing lanterns from a bundle of uniformly sized SMFs. Cladding index is set to 1.444, corresponding to fused silica at $1.55 \mu m$ wavelength, while jacket-cladding contrast is set to 5.5×10^{-3} ; these parameters are typical for lantern construction (private communication with S. Leon-Saval). Core index is set so that the mode field diameter is $\sim 7.5 \mu m$, matching OFS ClearLite 980 16 fiber. The main difference between our simulated standard and hybrid PLs is in lantern core diameter. In the standard non-selective variant, all SMF cores have the same diameter $(4.4 \mu m)$, while in the hybrid variant one SMF core is made $2 \mu m$ micron larger in diameter to accept the LP₀₁ mode. In either case, entrance diameter (i.e. the diameter of the cladding at the input MMF end of the lantern) is set to $20 \mu m$. Additionally, both lanterns have their lengths set by an optimization routine that maximizes for linearity in the lantern's intensity response to the first five non-piston Zernike aberrations. For more details on this procedure, see Lin et al (in prep).

Lastly, as a sanity check, we also simulate a fully mode-selective variant of the 6-port lantern, to verify our result from §3.1 that such lanterns are insensitive to all aberration modes. For simplicity, we assume that the modes of this lantern are exactly the first 6 LP modes, bypassing the need for numerical beam propagation.

5. RESULTS

In this section, we apply our numerical model to the standard, hybrid, and mode-selective 6-port lanterns. In §5.1, we look at the intensity response of these PLs, in the presence of selected static aberrations. These response curves can be thought of as 1D slices of the PLWFS response "surface" in the presence of many aberration modes. Subsections §5.2 and §5.3 compare the performances of the linear and quadratic reconstruction models.

5.1 Intensity response

Figure 4a shows the intensity response of a standard 6-port lantern as a function of mode amplitude for the first 5 (non-piston) Zernike modes. Empirically, we find that this is the maximum number of modes a 6-port lantern can sense. In Lin et al (in prep),²⁰ we find the more general result that an N-port PL can sense at most N-1 Zernikes, without additional optics. Our heuristic explanation is that the complex-valued response of an N-port PL is sensitive to piston, which takes up one degree of freedom out of the N total degrees in the system. This piston sensitivity is typically useless for wavefront sensing, and is lost if we measure the intensity instead of complex amplitude. Therefore, the PL is sensitive to at most N-1 Zernikes.

We additionally mark the regions where the linear approximation holds. This "linear range" is defined as the interval in Zernike mode amplitude within which the linear model reconstructs the original phase aberration with less than 0.1 radians RMS of error. Intensity responses to the tilt and astigmatism modes exhibit good linearity in the interval around [-0.4, +0.4] radians, while defocus exhibits linearity over a larger but more asymmetric range: around [-0.4, 0.8] radians. Note that the large linear range for defocus is primarily due to the taper length optimization outlined in §4.4. Conversely, certain values of taper length can lead to a lantern that is almost completely insensitive to defocus. We consider this and similar effects in more detail in Lin et al (in prep).⁷

Figure 4b shows intensity responses for a 6-port hybrid lantern against the same modes. The introduction of a single, larger lantern core changes the lantern mode structure, both by replacing one of the modes with the LP_{01} mode and by breaking the rotational symmetry of the lantern. We find that the 6-port hybrid lantern begins to behave non-linearly more quickly than its non-selective counterpart. Additionally, as seen in Figure 4c, a fully mode-selective 6-port lantern has completely symmetric intensity responses, and therefore is not useful for wavefront sensing. This simulated result corroborates our analytic result from Section §3.1. Finally, we find that our tested 6-port hybrid lanterns outperformed its standard counterpart in terms of degenerate radius (1.3 vs. 0.86 radians). This suggests that hybrid lanterns may exceed standard lanterns when using non-linear reconstruction methods.

Crucially, we emphasize that the above results are for a specific subset of 6-port lantern geometries. In Lin et al (in prep),²⁰ we extend these results to a wider range of PL designs.

5.2 Linear reconstruction

Given the intensity responses in Figures 4, computed over a range of Zernike mode amplitudes, we now apply the linear model (equation 13) in an attempt to reconstruct the original mode amplitude. Figure 5 plots reconstructed aberration mode amplitude against true mode amplitude for Zernike tilt, defocus, and astigmatism, both for a standard and hybrid 6-port lantern. From the Figure, we see that in terms of reconstruction range, the hybrid lantern performs worse than the standard lantern in all modes, particularly in astigmatism. This is in line with results from §5.1.

In order to test reconstruction performance in the presence of multiple aberrations, we use a Monte-Carlo approach. We first randomly draw 10,000 aberrated wavefronts (each composed of a random linear combination of Zernike modes 2-6), then pass each wavefront through our PLWFS model to obtain the corresponding intensity response. Given the intensity response, we attempt linear reconstruction. The root-mean-square of the difference between the "true" wavefront and the reconstructed wavefront gives an estimate of the overall accuracy of the reconstruction scheme. Figures 6a and b plots this accuracy against total aberration, for the standard and hybrid lantern, respectively. From the Figure, we see that reconstruction accuracy for the standard lantern remains

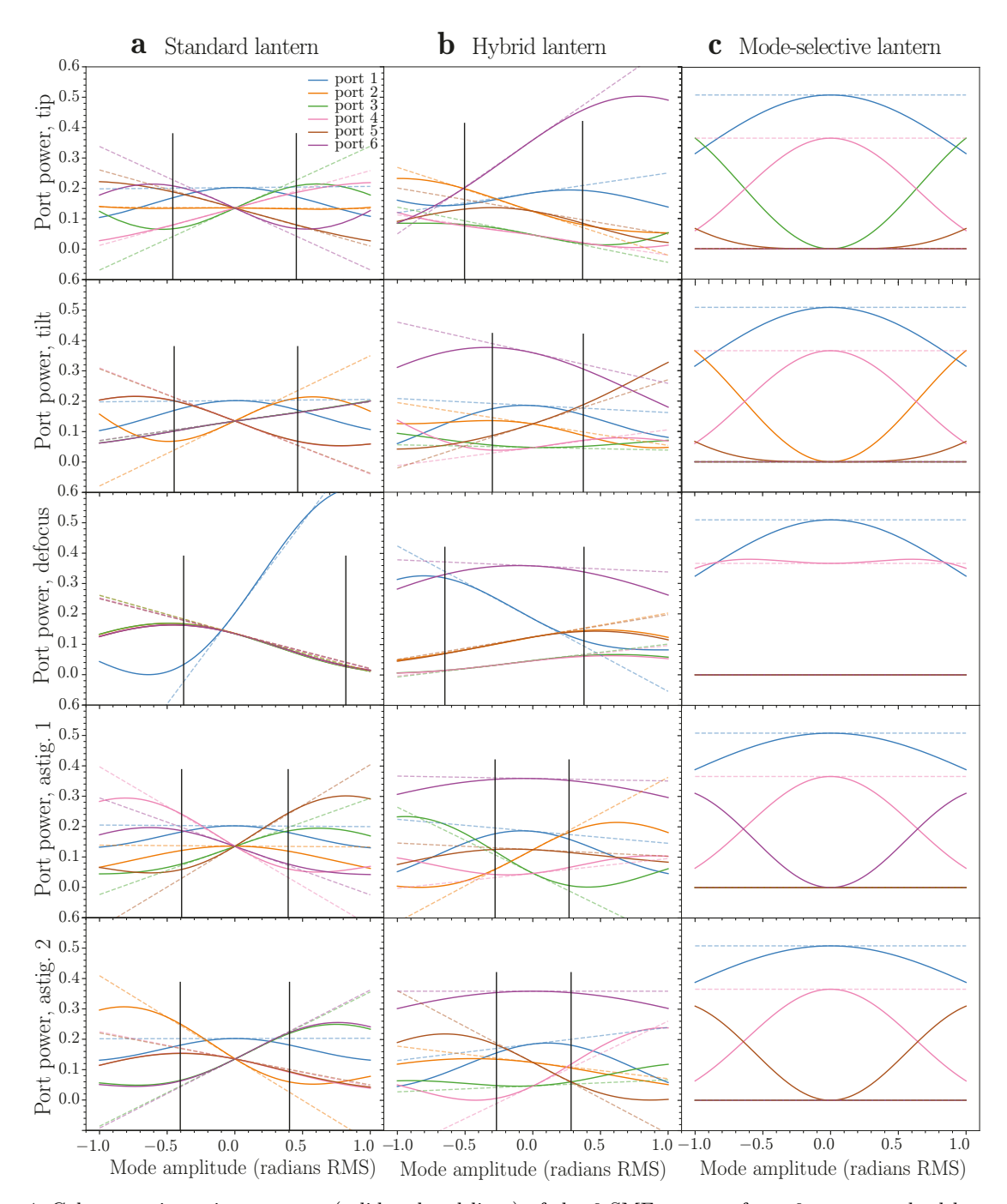


Figure 4. Column a: intensity response (solid, colored lines) of the 6 SMF outputs for a 6-port, standard lantern, as a function of aberration mode amplitude for Zernike modes 2-5 (tilt, defocus, and astigmatism). Vertical black lines denote the range where the linear model reconstructs the original aberration within 0.1 radians RMS. Dashed lines show the linear approximation for each port's response. Columns b, c: same as column a, but for a hybrid and mode-selective 6-port lantern, respectively.

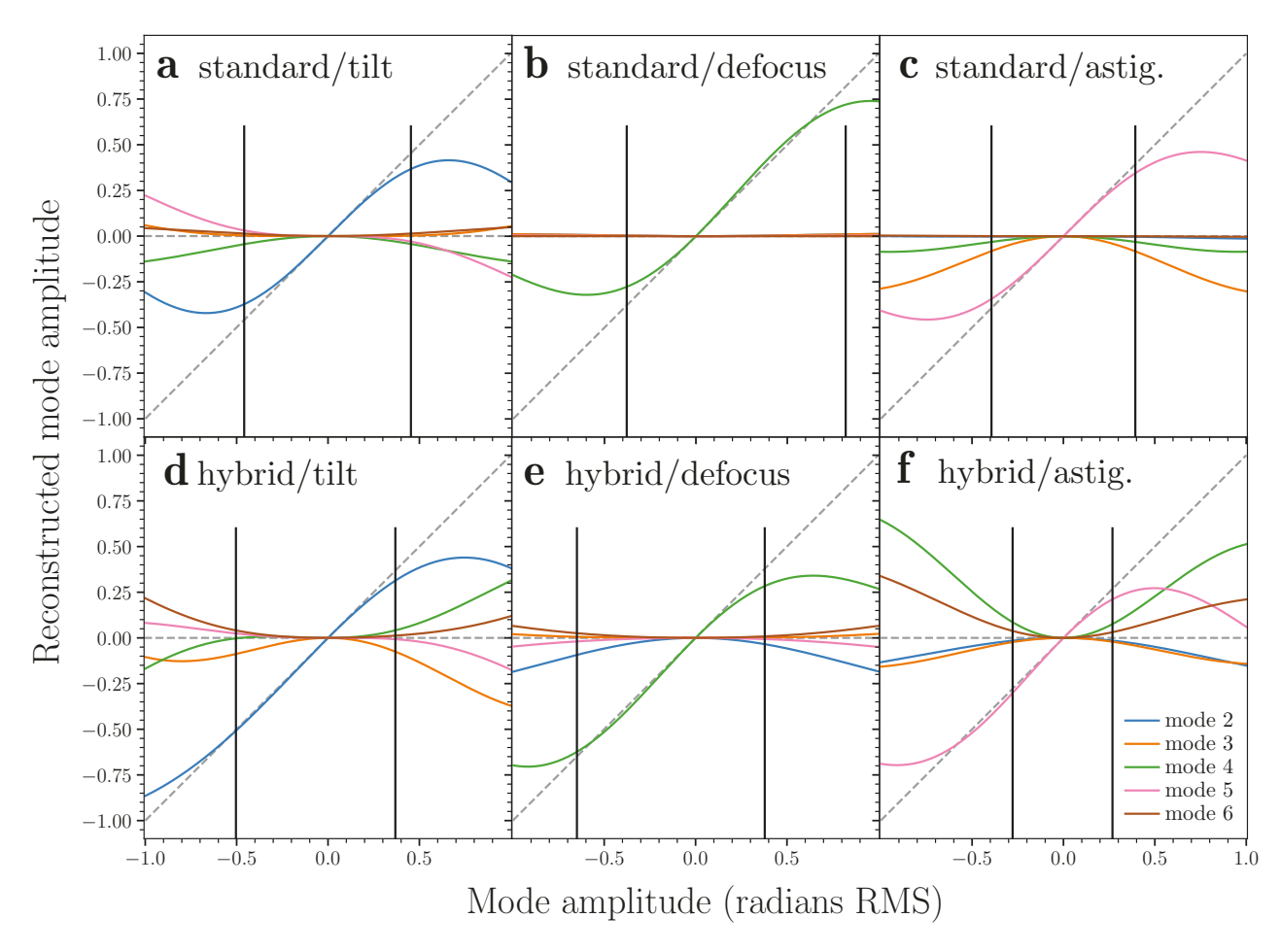


Figure 5. Panels a,b,c: Aberration reconstruction with the linear model, for various Zernike modes. Aberration amplitude is varied along the horizontal axis; this aberration is propagated into a lantern intensity response through our numerical model. We then attempt to do a linear reconstruction of the aberration amplitude, which we plot along the vertical axis. Under perfect reconstruction, the trace corresponding to the scanned mode should follow the line y=x (marked by the diagonal, dashed gray line) while all other traces should follow y=0 (flat, dashed gray line). As before, vertical black lines mark the region where linear reconstruction is accurate within 0.1 radians RMS. Panels d,e,f: the same as previous panels, but for a 6-port hybrid lantern.

under 0.1 radians for wavefront aberrations with up to ~ 0.35 radians of total RMS WFE; the hybrid lantern remains similarly accurate up to a lesser ~ 0.25 radians of total RMS WFE. While this result — that hybrid lanterns behave more non-linearly than standard lanterns — is specific to 6-port PLs, we find in Lin et al (in prep)²⁰ that it also applies for PLs of other sizes.

5.3 Quadratic reconstruction

In this subsection we present simulated results for the simplest non-linear reconstruction method: quadratic reconstruction. This method is based off equation 14, which we invert using the Levenberg-Marquardt root-finding algorithm as implemented by the Python package SciPy. For the initial guess required by the root-finder, we use the linearly reconstructed phase aberration vector.

We use the same Monte-Carlo approach outlined in the previous section to test the reconstruction performance of the quadratic model. Our results – reconstruction accuracy against total RMS WFE for 10,000 randomly sampled aberrations – are shown in Figure 6d and e, for the standard and hybrid 6-port lanterns, respectively. Comparing with panels a and b, which were generated using the linear reconstruction model, we see that the quadratic model lowers the overall error in wavefront reconstruction, as expected. Specifically, for the standard lantern, quadratic reconstruction allows aberrations with up to ~ 0.45 radians of total RMS WFE to be reconstructed to an accuracy of 0.1 radians RMS. The hybrid lantern is similarly accurate up to ~ 0.35 radians of total RMS WFE. These results represents a $\sim 30-40\%$ increase in reconstruction range over the linear model. Notably, the hybrid PL benefits more from quadratic reconstruction than the standard PL, which reinforces the notion that the hybrid PL behaves more non-linearly.

The quadratic model has the potential to provide even greater gains in reconstruction range when applied to PLs that behave more non-linearly than the 6-port lanterns tested in this work, whose lengths were specifically optimized to maximize linearity. To show this, we apply the linear and quadratic reconstruction models to a 6-port hybrid lantern without any linearity optimization. Results are shown in Figures 6c and f, respectively. The large spread and diverging pattern of points in panel c clearly shows the highly non-linear nature of this particular PL; nevertheless, when switching to quadratic reconstruction model in panel f, the reconstruction error for most aberrations drops dramatically. In scenarios where linearity optimization is infeasible, quadratic reconstruction may provide an alternate path to improving WFS performance.

However, the quadratic model is not without downsides. The major issue is that quadratic reconstruction tends to become increasingly numerically unstable as total RMS WFE increases. We see this behavior reflected in Figure 6 particularly in panels e and f, where the scatter of points increases substantially with increasing RMS WFE. These instabilities occur when the root-finder used to invert equation 14 gets stuck in a local extremum, or converges to a secondary solution (recall that equation 14 can admit multiple solutions). We discuss how this instability may be circumvented in Section §7.

Expansion of the lantern response to cubic order is given in Appendix B.

6. EXPANSION IN COMPLEX AMPLITUDE

So far, this work has expanded the wavefront aberration in phase, and has conducted analysis of the intensity response up to second order. When considering higher order effects, it may be more effective to instead expand in complex amplitude as follows:

$$E_{\rm in} \approx 1 + \delta E.$$
 (29)

The intensity response to second order in δE can be written as

$$I_{\text{out}} = |AE_{\text{in}}|^2,$$

$$\approx |A(\mathbf{1} + \delta E)|^2$$

$$I_{\text{out}} \approx |A\mathbf{1}|^2 + 2\operatorname{Re}\left[(A\mathbf{1}) \odot (A^* \delta E)\right] + |A\delta E|^2$$
(30)

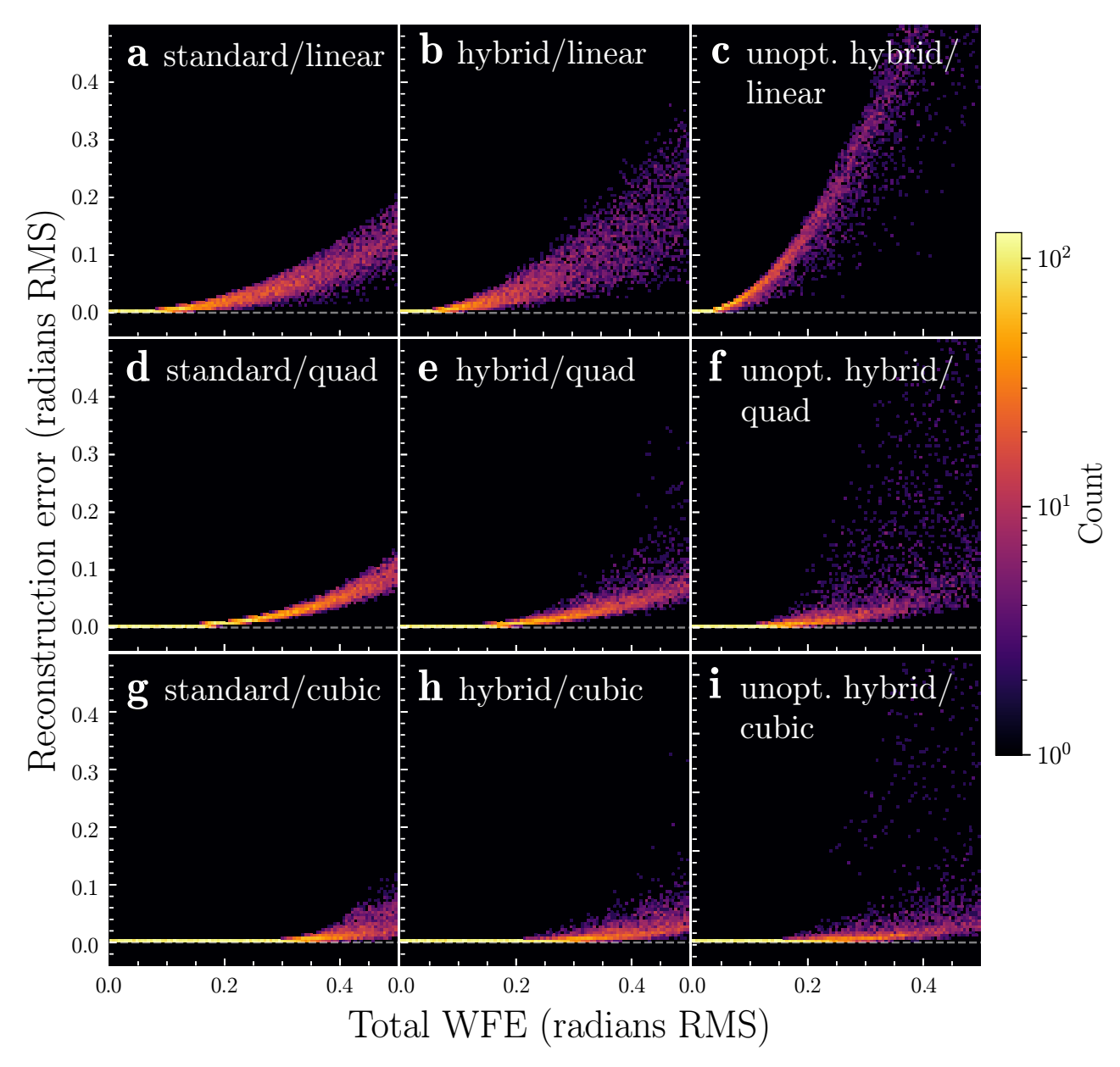


Figure 6. Panels a,d,g: heatmap of wavefront reconstruction accuracy against total RMS WFE for the standard 6-port lantern in the presence Zernike modes 2-5, using the linear, quadratic, and cubic reconstruction methods, respectively. Reconstruction accuracy was computed for 10,000 randomly sampled phase aberration vectors. A perfect wavefront sensor would have all reconstruction error along the line y = 0, shown by the dashed gray line. Panels b,e,h: same as the previous panels but for the hybrid 6-port lantern. Panels c,f,i: same as the previous panels but for a hybrid 6-port lantern without linearity-maximizing taper length optimization.

We can now define a matrix B, having the same dimensions as A, as

$$B_{ij} \equiv 2 \operatorname{Re} \left[A_{ij}^* \sum_{k} A_{ik} \right]. \tag{31}$$

Note that this is the element-wise complex conjugate of the B matrix when expanding in phase, corresponding to expressing the aberration in complex amplitude instead of phase, its approximate imaginary component.

We can also define a three-dimensional tensor C_{imn} as follows:

$$C_{imn} \equiv A_{ni}A_{mi}^* + A_{mi}A_{ni}^*. \tag{32}$$

The intensity response to second order in complex amplitude can now be expressed as

$$I_{\text{out}} = |A\mathbf{1}|^2 + B\delta \mathbf{E} + \delta \mathbf{E}^T C\delta \mathbf{E}. \tag{33}$$

Future work will explore how this expansion in complex amplitude can be leveraged for quadratic wavefront sensing with photonic lanterns. This expansion in complex amplitude may provide several advantages: the expression for intensity is only quadratic in δE , so analysis beyond second order is not needed; the B matrix and C tensor have simple, analytical forms; and amplitude aberrations can be considered in this framework as well as phase. However, expanding in complex amplitude requires an additional calculation to obtain the phase from the electric field, so if the focus of wavefront sensing is on phase aberrations that can be corrected by a deformable mirror in the pupil plane, the second-order expansion in phase explored in §2.3 may be more appropriate.

7. DISCUSSION

In Section §2, we laid out a general mathematical framework for the intensity response of a WFS to errors in phase. While we recover the usual linear model in our first-order expansion, we additionally derive a quadratic reconstruction model. This model can improve reconstruction accuracy, especially for PLs: the general nonlinearity of these devices often leads to quadratic-like intensity responses which are not well-fit by the linear model. However, the added accuracy of this scheme is offset by increased complexity. For one, the photonic lantern's response can become degenerate in this regime, such that two distinct phase aberrations can map to the same intensity response. This degeneracy makes inverting the model more numerically unstable, especially for large amounts of total RMS WFE. Furthermore, the inversion from intensity back to aberration phase is most straightforwardly done with a numerical root-solver. This makes the quadratic model slower than the linear model, which only requires a single, fast matrix multiplication. It remains to be seen whether the increased accuracy afforded by the quadratic and higher order models outweigh the penalties in numerical stability and computation time, and if these techniques can be applied to closed-loop operation. We expect additional complications when moving to wavefront reconstruction with real PLWFSs. For one, we will have to contend with detector and photon noise, which will degrade both sensitivity and reconstruction range. Noise will likely be particularly problematic at the kHz refresh rates typically used for atmospheric compensation, but may be less of an issue when sensing slower NCPAs. An additional complication is that, in practice, the complex-valued A matrix must be experimentally determined (e.g. through phase diversity methods), and hence will be prone to the effects of random and systematic uncertainties. While linear reconstruction, which requires only intensity knowledge, will be largely unaffected, uncertainties in A may make non-linear reconstruction even more numerically unstable. These uncertainties may be mitigated if we can constrain the A matrix (for instance, through its modulus, or through B).

We imagine several potential next steps in our mathematical analysis. One interesting continuation is to extend our phase-only aberration analysis to amplitude aberrations as well. Another is the expansion of WFS intensity response to third order, which we begin in Appendix B; see also Figure 6g-i, which plots the similar reconstruction heatmaps as panels a-f but for a cubic reconstruction model. Cubic expansion is particularly interesting because many PL intensity response functions (e.g. for the 6-port standard lantern, Figure 4a) appear predominantly

cubic. Figure 6 confirms that this expansion can offer a significant boost in reconstruction accuracy, especially for the 6-port standard lantern. However, the drawbacks are similar to the quadratic model. Each increase in order is accompanied by an increase in the model degeneracy, as well as an increase in the rank of the tensors required by the model. Future work will also explore expanding in complex amplitude instead of phase, which results in an expression for intensity that is only second-order in wavefront error, and has the potential to account for amplitude aberrations as well.

More advanced reconstruction models may overcome the drawbacks of higher order analysis. One idea is to use wavelength diversity, leveraging the chromatic dependence of the PLWFS response. Intuitively, we expect that measurements of the PLWFS response at two separate wavelengths would be enough to enable the inversion of the quadratic model. These measurements can be made though spectral dispersion of the PLWFS outputs, as in the so-called photonic "TIGER" configuration. Lastly, we emphasize that while going to higher order may amplify numerical instability, it does not amplify experimental uncertainties in the A matrix; this is because intensity will always have a second-order dependence on complex amplitude.

Besides enabling wavefront reconstruction, mathematical models have a second, important use: they allow us to derive certain WFS properties and metrics through which the WFS can be optimized. For instance, in §3.1, we derived that a fully mode-selective lantern is insensitive to phase aberrations, for even pupil transmission. It remains to be shown whether or not this limitation can be practically overcome with pupil masks or other additional optics. In contrast, there are no such restrictions with standard and hybrid lanterns. As a corollary, we found that the linearity of the PLWFS, at least for small aberrations, depends on the phase of what we call the Q metric (equation 25). We also show how this linearity condition simplifies for certain cases, such as the 6-port standard PL in the presence of defocus (Appendix A). In the future, it may be desirable to optimize the PLWFS for this linearity condition. However, if non-linear reconstruction methods, such as the quadratic or cubic methods in this work or the neural-net approach from, ¹⁴ can be developed that are fast and stable enough to compete with linear reconstruction, it may instead be desirable to optimize lanterns according to "degenerate radius" (equation 27). Both the linear Q metric and the degenerate radius are only the first steps in analytically defining the sensing properties of the PLWFS. Next steps will be to derive expressions for other potentially more useful properties, such as linear range (different from our condition 25, which only ensures local linearity about the origin). Collectively, these analytically-derived expressions will help inform the manufacture of real PLWFSs in the future.

Finally, we used our mathematical models to numerically simulate and compare the wavefront-sensing performance of an idealized standard, hybrid, and mode-selective 6-port PL. As expected, we recovered our analytic result that the mode-selective PL under even pupil illumination is insensitive to phase aberrations. We also found that the hybrid PL behaved more non-linearly than the standard PL, suggesting that the latter may make a better wavefront sensor if used with a linear reconstruction scheme. In contrast, the larger degenerate radius of the 6-port hybrid lantern may make it a better choice with non-linear reconstruction schemes. The next step will be to improve our model accuracy by accounting for manufacturing imperfections in simulated PLs, and to verify these models on an experimental testbed.

8. CONCLUSIONS

In this work, we provide an end-to-end mathematical analysis of the PLWFS. In Sections §2 and §3, we developed linear and higher-order mathematical models for the intensity response of the PLWFS. These models enable the reconstruction of wavefront aberrations from intensity responses, and enable the derivation of certain metrics, such as the degenerate radius, which estimates the maximum amount of RMS WFE an aberration can have before the mapping of aberrations to intensities is no longer one-to-one. Such metrics can be used to benchmark and control the sensing behavior of these devices. Higher-order reconstruction models, such as quadratic (§2.3 and §5.3) and cubic (Appendix B), can additionally enable greatly improved reconstruction accuracy over the the standard linear model, but at the cost of added computation time and potentially increased numerically instability. Through our framework, we also show that a fully mode-selective lantern cannot sense wavefront aberrations with even pupil illuminations.

As a proof-of-concept, we apply our reconstruction models to a standard, hybrid, and mode-selective 6-port lantern in Section §5, and successfully show that for the first two cases wavefront reconstruction of the first 5 non-piston Zernike modes is possible; 5 is the maximum number modes that can be sensed by either 6-port variant. We additionally confirm, numerically, that mode-selectivity (at least with an even pupil) hinders wavefront sensing. Comparing the performance of the standard and hybrid lanterns at a single output wavelength of 1.55 μ m, we find that the standard lantern has the highest linear range, accurately sensing the first five non-piston Zernike modes out to ~ 0.5 radians, followed by the hybrid lantern. Conversely, the 6-port hybrid PL outperformed the standard PL in terms of degenerate radius. In the second part of this paper, we extend our analysis and simulate reconstruction performance for a range of PLs in various configurations. We additionally provide initial investigations into new strategies through which the sensing properties of PLs can be controlled and optimized. In the near future, we hope to verify our results with real, imperfect photonic lanterns, through experimental and on-sky testing, and in doing so, add to the next generation of focal-plane wavefront sensors.

APPENDIX A. DEFOCUS PERFORMANCE FOR STANDARD 6-PORT LANTERN

The linearity criterion from §3.3 can be simplified for a standard 6-port lantern, located in the focal plane of a telescope with a filled circular aperture, in the presence of defocus. We order our basis of LP modes as (LP₀₁, LP₀₂, rest of the LP modes) and our output ports as (central port, rest of the ports). Due to symmetry, both an unaberrated wavefront and a defocused wavefront will only couple into LP₀₁ and LP₀₂. Furthermore, the coupling coefficients will be real. Therefore, we can set

$$P\mathcal{F}\mathbf{1} \equiv \begin{pmatrix} a \\ b \\ 0 \\ \vdots \end{pmatrix}, P\mathcal{F}\mathbf{z} \equiv \begin{pmatrix} d \\ f \\ 0 \\ \vdots \end{pmatrix}$$

$$(34)$$

where a, b, c, d are real numbers and z is the vector corresponding to the defocus mode. Denoting the columns of the lantern propagation matrix U as c_i , we find that equation 25 becomes

$$Q = ad|\mathbf{c}_1|^2 + af\mathbf{c}_1 \odot \mathbf{c}_2^* + bd\mathbf{c}_2 \odot \mathbf{c}_1^* + bf|\mathbf{c}_2|^2.$$
(35)

We want Q to be "as imaginary as possible". Clearly, the first and last terms are real, so a lantern that satisfies

$$ad|c_1|^2 + bf|c_2|^2 = 0 (36)$$

will behave "more linearly" than one that doesn't. The middle terms apply another condition: the each element in c_1 should be 90° out of phase with its corresponding element in c_2 . In turn, this condition implies that the LP₀₁ and LP₀₂ components for each lantern mode must be 90° out of phase. We have verified this behavior numerically.

It is also useful to consider the converse of the above conclusion. Suppose that the LP₀₁ and LP₀₂ mode coefficients are in phase. Then, $c_1 \odot c_2^*$ will be real, and Q will be purely real. Consequently, the linear B matrix will be 0 - lantern response is purely quadratic.

APPENDIX B. CUBIC EXPANSION

Expand the incident electric field as

$$E_{\rm in} = 1 + i\phi - \frac{1}{2}\phi^2 - \frac{i}{6}\phi^3 + o(\phi^4). \tag{37}$$

As before, the intensity response of the WFS is

$$I_{\text{out}} = |AE_{\text{in}}|^2 \tag{38}$$

where A is the complex-valued transfer matrix of the overall optical system. Combining the above two equations and keeping only terms up to third order yields

$$I_{\text{out}} \approx I_{\text{out, quad}} - \frac{1}{3} \text{Im} \left[A \mathbf{1} \odot A^* \phi^3 \right] + \text{Im} \left[A \phi \odot A^* \phi^2 \right]$$
 (39)

where $I_{\text{out, quad}}$ is the quadratic approximation for output intensity, as per equation 10. We now expand the above model to an arbitrary modal basis. Let R be a change-of-basis matrix, such that $\phi = Ra$. The additional terms from the cubic expansion can be expressed as a single tensor multiplication of the form

$$\sum_{lmn} D'_{ilmn} a_l a_m a_n \tag{40}$$

where the tensor D'_{ilmn} is defined as

$$D'_{ilmn} = \text{Im} \left[-\frac{1}{3} \sum_{j} A_{ij} \sum_{k} A^*_{ik} R_{kl} R_{km} R_{kn} + \sum_{jk} A_{ij} A^*_{ik} R_{jl} R_{km} R_{kn} \right]. \tag{41}$$

The D' tensor has dimensions $N \times M \times M \times M$ for an N-port lantern sensing M aberration modes. The full cubic model, in modal basis, is

$$I_{\text{out},i} \approx |A\mathbf{1}|_i^2 + (B'\mathbf{a})_i - \frac{1}{2} \sum_{ik} C'_{ijk} a_j a_k + |A'\mathbf{a}|_i^2 + \sum_{lmn} D'_{ilmn} a_l a_m a_n$$
 (42)

Brief empirical testing with this model shows that it can provide a significant increase in reconstruction accuracy, especially for PLs that have already been optimized for linearity. Heatmaps of reconstruction error against total RMS WFE for 10,000 randomly sampled aberrations are shown in Figure 6g, h, and i, for various 6-port lantern designs. Notably, going to higher order consistently extends the reconstruction range of the sensor, suggesting that the main downside of higher-order models is the additional computational complexity, rather than numerical instability.

ACKNOWLEDGMENTS

This material is based upon work supported by the National Science Foundation Graduate Research Fellowship Program under Grant Numbers DGE-2034835 and 1122374. Any opinions, findings, and conclusions or recommendations expressed in this material are those of the author(s) and do not necessarily reflect the views of the National Science Foundation. This work was also supported by the National Science Foundation under Grant No. 2109232.

REFERENCES

- [1] Marois, C., Lafreniere, D., Doyon, R., Macintosh, B., and Nadeau, D., "Angular differential imaging: A powerful high-contrast imaging technique," The Astrophysical Journal **641**, 556–564 (apr 2006).
- [2] Sparks, W. B. and Ford, H. C., "Imaging spectroscopy for extrasolar planet detection," <u>The Astrophysical</u> Journal 578, 543-564 (2002).
- [3] Bowler, B. P., "Imaging extrasolar giant planets," <u>Publications of the Astronomical Society of the Pacific 128</u>, 102001 (aug 2016).
- [4] Martinez, P., Loose, C., Aller Carpentier, E., and Kasper, M., "Speckle temporal stability in xao coronagraphic images," A&A **541**, A136 (2012).
- [5] Martinez, P., Kasper, M., Costille, A., Sauvage, J. F., Dohlen, K., Puget, P., and Beuzit, J. L., "Speckle temporal stability in xao coronagraphic images - ii. refine model for quasi-static speckle temporal evolution for vlt/sphere," A&A 554, A41 (2013).
- [6] Traub, W. A. and Oppenheimer, B. R., "Direct Imaging of Exoplanets," in [Exoplanets], Seager, S., ed., 111–156 (2010).

- [7] Lin, J., Jovanovic, N., and Fitzgerald, M. P., "Design considerations of photonic lanterns for diffraction-limited spectrometry," J. Opt. Soc. Am. B 38, A51–A63 (Jul 2021).
- [8] Birks, T. A., Gris-Sánchez, I., Yerolatsitis, S., Leon-Saval, S. G., and Thomson, R. R., "The photonic lantern," Adv. Opt. Photon. 7, 107–167 (Jun 2015).
- [9] "GNOSIS: The first instrument to use fiber Bragg gratings for OH suppression," The Astronomical Journal 145, 51 (jan 2013).
- [10] Ellis, S. C., Bauer, S., Bacigalupo, C., Bland -Hawthorn, J., Bryant, J. J., Case, S., Content, R., Fechner, T., Giannone, D., Haynes, R., Hernandez, E., Horton, A. J., Klauser, U., Lawrence, J. S., Leon-Saval, S. G., Lindley, E., Löhmannsröben, H. G., Min, S. S., Pai, N., Roth, M., Shortridge, K., Waller, L., Xavier, P., and Zhelem, R., "PRAXIS: an OH suppression optimised near infrared spectrograph," in [Proceedings of the SPIE], Society of Photo-Optical Instrumentation Engineers (SPIE) Conference Series 10702, 107020P (Jul 2018).
- [11] Gatkine, P., Veilleux, S., and Dagenais, M., "Astrophotonic spectrographs," Applied Sciences 9(2) (2019).
- [12] Leon-Saval, S. G., Fontaine, N. K., Salazar-Gil, J. R., Ercan, B., Ryf, R., and Bland-Hawthorn, J., "Mode-selective photonic lanterns for space-division multiplexing," Opt. Express 22, 1036–1044 (Jan 2014).
- [13] Corrigan, M. K., Morris, T. J., Harris, R. J., and Anagnos, T., "Demonstration of a photonic lantern low order wavefront sensor using an adaptive optics testbed," in [Adaptive Optics Systems VI], Close, L. M., Schreiber, L., and Schmidt, D., eds., 10703, 1313 1320, International Society for Optics and Photonics, SPIE (2018).
- [14] Norris, B. R. M., Wei, J., Betters, C. H., Wong, A., and Leon-Saval, S. G., "An all-photonic focal-plane wavefront sensor," Nature Communications 11, 5335 (Oct 2020).
- [15] Wright, T. A., Yerolatsitis, S., Harrington, K., Harris, R. J., and Birks, T. A., "All-fibre wavefront sensor," (2022).
- [16] Ruane, G., Echeverri, D., Jovanovic, N., Mawet, D., Serabyn, E., Wallace, J. K., Wang, J., and Batalha, N., "Vortex fiber nulling for exoplanet observations: conceptual design, theoretical performance, and initial scientific yield predictions," in [Techniques and Instrumentation for Detection of Exoplanets IX], Shaklan, S. B., ed., 11117, 366 381, International Society for Optics and Photonics, SPIE (2019).
- [17] Mawet, D., Fitzgerald, M., Konopacky, Q., Beichman, C., Jovanovic, N., Dekany, R., Hover, D., Chisholm, E., Ciardi, D., Artigau, E., Banyal, R., Beatty, T., Benneke, B., Blake, G. A., Burgasser, A., Canalizo, G., Chen, G., Do, T., Doppmann, G., Doyon, R., Dressing, C., Fang, M., Greene, T., Hillenbrand, L., Howard, A., Kane, S., Kataria, T., Kempton, E., Knutson, H., Kotani, T., Lafreniere, D., Liu, C., Nishiyama, S., Pand ey, G., Plavchan, P., Prato, L., Rajaguru, S. P., Robertson, P., Salyk, C., Sato, B., Schlawin, E., Sengupta, S., Sivarani, T., Skidmore, W., Tamura, M., Terada, H., Vasisht, G., Wang, J., and Zhang, H., "High-resolution Infrared Spectrograph for Exoplanet Characterization with the Keck and Thirty Meter Telescopes," arXiv e-prints, arXiv:1908.03623 (Aug 2019).
- [18] Guyon, O., "Phase-induced amplitude apodization of telescope pupils for extrasolar terrestrial planet imaging," A & A **404**(1), 379–387 (2003).
- [19] Paschotta, R., "Lp modes," (Jan 2022).
- [20] Lin, J. and Fitzgerald, M., "Focal-plane wavefront sensing with photonic lanterns ii: characterization and optimization," in prep. (2022).
- [21] Por, E. H., Haffert, S. Y., Radhakrishnan, V. M., Doelman, D. S., van Kooten, M., and Bos, S. P., "High Contrast Imaging for Python (HCIPy): an open-source adaptive optics and coronagraph simulator," in [Adaptive Optics Systems VI], Close, L. M., Schreiber, L., and Schmidt, D., eds., 10703, 1112 1125, International Society for Optics and Photonics, SPIE (2018).
- [22] Lin, J. W., "Lightbeam." Astrophysics Source Code Library (Feb. 2020). ascl:2102.006.
- [23] Leon-Saval, S. G., Betters, C. H., and Bland-Hawthorn, J., "The Photonic TIGER: a multicore fiber-fed spectrograph," in [Modern Technologies in Space- and Ground-based Telescopes and Instrumentation II], Navarro, R., Cunningham, C. R., and Prieto, E., eds., 8450, 550 557, International Society for Optics and Photonics, SPIE (2012).